Chemical Science

ROYAL SOCIETY OF CHEMISTRY

EDGE ARTICLE

View Article Online
View Journal | View Issue

Check for updates

Cite this: *Chem. Sci.*, 2024, **15**, 15192

All publication charges for this article have been paid for by the Royal Society of Chemistry

Received 25th June 2024
Accepted 24th August 2024

DOI: 10.1039/d4sc04185b

rsc.li/chemical-science

Achievement of a giant electromechanical conversion coefficient in a molecule-based ferroelectric†

Bin Wang,‡ Zhirui Li,‡ Zhengxiao Tang, Haixia Zhao, * Lasheng Long * and Lansun Zheng

Molecule-based ferroelectrics are promising candidates for flexible self-powered power supplies (*i.e.*, piezoelectric generators (PEGs)). Although the large electromechanical conversion coefficients ($d_{33} \times g_{33}$) of piezoelectrics are key to enhancing the performance of PEGs in their nonresonant states, it remains a great challenge to obtain molecule-based piezoelectrics with large $d_{33} \times g_{33}$. Here, we report a molecule-based ferroelectric $[(CH_3)_3NCH_2CH_2Cl][GaBr_4]$ (**1**) that exhibits the largest piezoelectric coefficient (~454 pC N^{-1}) and electromechanical conversion coefficient (4953.1 × 10^{-12} m^2 N^{-1}) among all known free-standing polycrystalline pellets. Notably, the PEG comprising 15 wt% **1** and polydimethylsiloxane (PDMS) achieves a power density of up to 120 μW cm^{-2}, marking the highest reported power density for ferroelectric@PDMS PEGs to date.

Introduction

Flexible wearable devices are an inevitable trend in the intelligent era.[1–4] However, the low power densities of flexible self-powered power supplies have restricted their development.[5] Because piezoelectric generators (PEGs) can directly convert mechanical energy into electrical energy and *vice versa*,[6–8] they are considered promising self-powered power suppliers.[9] According to eqn (1),[10–12]

$$u = \frac{1}{2}(d_{33} \times g_{33})\left(\frac{F}{A}\right)^2 \quad (1)$$

(where u, d_{33}, g_{33}, F and A are the energy density, piezoelectric coefficient, piezoelectric voltage coefficient, applied force, and stress area, respectively, and u is obviously determined by the electromechanical conversion coefficient ($d_{33} \times g_{33}$)), a large $d_{33} \times g_{33}$ is key to improve the performance of PEGs in the nonresonant state.[13] Inorganic piezoelectric materials tend to exhibit large d_{33} values, but they often suffer from small g_{33} values and high stiffness. Organic piezoelectric materials, on the other hand, tend to display large g_{33} values and mechanical flexibility, but they often have small d_{33} values. Therefore, it is a great challenge to obtain flexible piezoelectric materials with large $d_{33} \times g_{33}$ and mechanical flexibility based only on inorganic or organic piezoelectric materials.

With the use of both organic and inorganic units in the same molecule, molecule-based ferroelectrics are expected to combine the light weight and flexibility of organic piezoelectric materials with the mechanical strength and toughness of inorganic piezoelectric materials and exhibit large $d_{33} \times g_{33}$ and mechanical flexibility.[14] Although recent studies have shown that there are indeed very few molecule-based ferroelectrics that exhibit large $d_{33} \times g_{33}$ and mechanical flexibility,[2,15,16] their $d_{33} \times g_{33}$ values were recorded specifically along certain axial directions of single crystals. In contrast, the $d_{33} \times g_{33}$ values of molecule-based ferroelectrics obtained from free-standing polycrystalline pellets are relatively small, despite that the large $d_{33} \times g_{33}$ value for free-standing polycrystalline pellets of molecule-based ferroelectrics is of key importance for their practical application, especially in flexible wearable devices. Here, we report the molecule-based ferroelectric $[(CH_3)_3NCH_2CH_2Cl][GaBr_4]$ (**1**), which exhibits the largest $d_{33} \times g_{33}$ (4953.1 × 10^{-12} m^2 N^{-1}) among known free-standing polycrystalline pellets, and this demonstrates that the key to obtaining molecule-based ferroelectrics with large $d_{33} \times g_{33}$ values lies in using more flexible organic cations with larger dipole moments to construct ferroelectric materials with multiaxial characteristics.

Results and discussion

Crystal structure of 1

Compound **1** was prepared through a reaction of gallium(III) oxide and (2-chloroethyl)trimethylammonium chloride in HBr.

Collaborative Innovation Center of Chemistry for Energy Materials, State Key Laboratory of Physical Chemistry of Solid Surfaces and Department of Chemistry, College of Chemistry and Chemical Engineering, Xiamen University, Xiamen, 361005, Fujian, China. E-mail: hxzhao@xmu.edu.cn; lslong@xmu.edu.cn

† Electronic supplementary information (ESI) available. CCDC 2190250. For ESI and crystallographic data in CIF or other electronic format see DOI: https://doi.org/10.1039/d4sc04185b

‡ These authors contributed equally to this work.

Open Access Article. Published on 28 August 2024. Downloaded on 6/21/2025 3:22:39 AM. This article is licensed under a Creative Commons Attribution-NonCommercial 3.0 Unported Licence.

© 2024 The Author(s). Published by the Royal Society of Chemistry

Open Access Article. Published on 28 August 2024. Downloaded on 6/21/2025 3:22:39 AM. This article is licensed under a Creative Commons Attribution-NonCommercial 3.0 Unported Licence.

Single crystal structural analysis revealed that **1** crystallized in the orthomorphic polar space group $Pca2_1$ at room temperature, and the cell parameters are $a = 14.0655(8)$ Å, $b = 7.6705(5)$ Å, $c = 13.2164(7)$ Å, and $Z = 4$ (Table S1†). The asymmetric unit of **1** consists of one $[(CH_3)_3NCH_2CH_2Cl]^+$ cation and one $[GaBr_4]^-$ anion (Fig. S1†). The experimental powder X-ray diffraction (PXRD) patterns align closely with those simulated from the crystal structure at room temperature (Fig. S2†), confirming the purity of **1**. Each $[(CH_3)_3NCH_2CH_2Cl]^+$ cation is encircled by four $[GaBr_4]^-$ anions, and *vice versa*, interconnected through Coulomb and van der Waals forces to form the three-dimensional structure of **1**, as illustrated in Fig. 1. Because the distances between the Br atoms of $[GaBr_4]^-$ anions and the surrounding non-hydrogen atoms are more than 3.50 Å (Table S2†), the intermolecular forces in **1** are mainly due to Coulomb force and van der Waals force among the ions. Consequently, the $[(CH_3)_3NCH_2CH_2Cl]^+$ cation exhibits significant conformational flexibility, with the two carbon atoms in the side chain of the cation displaying orientational disorder across two positions (Fig. S1†). Thermogravimetric (TG) analysis and differential scanning calorimetry (DSC) (Fig. S3 and S4a†) reveal that **1** is stable up to 550 K, with no phase transition before melting at 485 K (Fig. S4b†). This behavior is due to the presence of a long side chain and a heavy Cl atom in the $[(CH_3)_3NCH_2CH_2Cl]^+$ cation, which collectively contributes to a high tumbling energy barrier for the $[(CH_3)_3NCH_2CH_2Cl]^+$ cation.

Piezoelectric properties of 1

Because **1** crystallizes in the polar space group $Pca2_1$, second harmonic generation (SHG) was measured with a polycrystalline sample. As shown in Fig. S5a,† the SHG intensity was approximately ~1.52 times that of potassium dihydrogen phosphate (KDP) with the same particle sizes. And the SHG-temperature dependence (Fig. S5b†) reveals that the SHG intensity remains stable until it melts. Due to the high SHG activity of **1**, the d_{33} of a free-standing polycrystalline pellet was determined by a quasi-static method. The d_{33} of 454 pC N^{-1} with forward and reverse connections (Fig. S6†) determined for **1** is comparable to those of high-piezoelectric performance PZT (300–510 pC N^{-1}).[6] Although some molecule-based ferroelectrics reported previously exhibit the highest d_{33} along specific directions in single crystal samples, such as $(TMFM)_x(TMCM)_{1-x}CdCl_3$ solid solutions,[1] to the best of our knowledge, **1** is the largest d_{33} obtained to date for a free-standing polycrystalline pellet of a molecule-based ferroelectric material (Table S3†). To further confirm the piezoelectric properties of **1**, its strain–electric field curve was measured. As shown in Fig. 2a, the typical butterfly shaped *S*–*E* curve for a free-standing polycrystalline pellet exhibit both positive and negative strains, and the strain signs were independent of the direction and magnitude of the applied field in the *S*–*E* curve of **1**, indicating the presence of domain wall motion and/or domain reversal.[17–19] Based on $d^*_{33} = S_{max}/E_{max}$,[20] the piezoelectric coefficient (d^*_{33}) of **1** was approximately 505 pm V^{-1}. The d^*_{33} greater than d_{33} can be attributed to the combined piezoelectric effect and pure electrostrictive effect.[17–20] The large d^*_{33} further confirms that **1** possesses excellent piezoelectric properties. According to the frequency-dependent relative permittivity at room temperature (Fig. S7†), the g_{33} for **1** is approximately 10 910 × 10^{-3} V m N^{-1} based on $g_{33} = d_{33}/\varepsilon_{33}$, where the ε_{33} value is chosen at the 10 kHz frequency rather than at extremely low frequencies (below 100 Hz) to avoid the contribution of space charge polarization at the electrode interface.[21] It is worth mentioning that the g_{33} value of **1** is significantly larger than that of PVDF (286.7 × 10^{-3} V m N^{-1})[22] and represents the largest g_{33} reported to date (Table S3†). Fig. 2b lists the $d_{33} \times g_{33}$ values of excellent piezoelectric materials reported to date and commercial piezoelectric materials. The calculated $d_{33} \times g_{33}$ for **1** is as high as 4953.1 × 10^{-12} m^2 N^{-1}. This value is significantly larger than those observed for commercial piezoelectric materials and also larger than those observed for the molecule-based piezoelectric materials $TMCMGaCl_4$,[16] $TMCM_2SnCl_6$,[2] and $(PTMA)CdBr_2Cl_{1-x}I_x$ (TMCM = $(CH_3)_3NCH_2Cl^+$; PTMA = $C_6H_5N(CH_3)_3^+$).[21] In fact, the $d_{33} \times g_{33}$ for a free-standing polycrystalline pellet **1** is second only to that of single crystalline $(TMFM)_x(TMCM)_{1-x}CdCl_3$ ($x = 0.26$, $d_{33} = 1540$

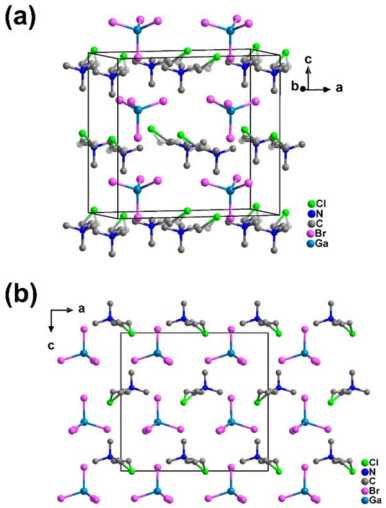

Fig. 1 Crystal structure of **1**. (a) Unit cell of **1** at room temperature. (b) Stacked structure of **1** viewed along the *b* axis at room temperature.

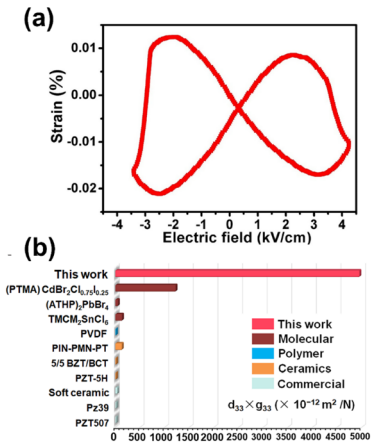

Fig. 2 Piezoelectric properties of **1**. (a) *S*–*E* curves of **1**. (b) $d_{33} \times g_{33}$ of **1** compared with those of other reported piezoelectric materials.

Open Access Article. Published on 28 August 2024. Downloaded on 6/21/2025 3:22:39 AM. This article is licensed under a Creative Commons Attribution-NonCommercial 3.0 Unported Licence.

pC N^{-1}) (Table S4†). Hence, the $d_{33} \times g_{33}$ in **1** is the largest reported to date for a free-standing polycrystalline pellet piezoelectric material.

To reveal the intrinsic nature of the piezoelectric properties of **1**, a polycrystalline film of **1** was examined with piezoelectric response force microscopy (PFM) in different areas at room temperature. As shown in Fig. 3a, b and S8,† the static ferroelectric domain structure and walls of **1** were observed in both the longitudinal and transverse PFM modes, and there is no crosstalk between the domain distributions and the corresponding morphologies in the longitudinal and transverse PFM modes (Fig. S9†). These results indicate that **1** has multiaxial characteristics. Consistently, the characteristic butterfly amplitude-voltage loops and square phase-voltage loops observed in Fig. 3c and d through switching spectroscopy PFM (SS-PFM) confirm the reversal of ferroelectric polarization in **1**. Fig. S10a and b† demonstrate reversible polarization switching in response to the electric field. And the topography image in Fig. S10c† shows no signs of ablation in the area where reversible polarization switching occurs. Moreover, as depicted in the amplitude images and phase images overlaid on the 3D topography (Fig. S10d and e†), the reversible polarization switching is controlled by the electric field without any modification of the sample topography, further demonstrating the ferroelectricity of **1**. Furthermore, the polarization–electric field (*P*–*E*) hysteresis loop measurements are carried out on a polycrystalline film of **1**, and the positive up negative down (PUND) method is employed to eliminate leakage currents (Fig. S11†). As shown in Fig. 4, the *P*–*E* hysteresis loop and current density electric field (*J*–*E*) curve all confirm that **1** is a molecule-based ferroelectric. The saturated polarization (P_s) is 9.5 μC cm^{-2}, close to the theoretical value (11.3 μC cm^{-2}) which is determined by Gaussian09 software at the B3LYP/def2TZVP level of theory.

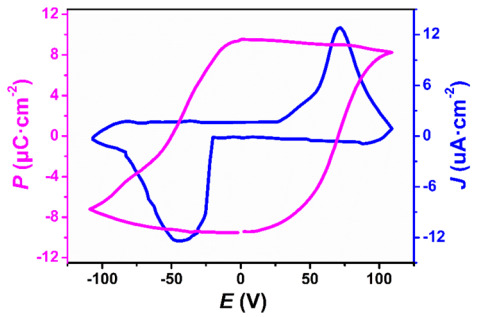

Fig. 4 The *P*–*E* hysteresis loop and *J*–*E* curve of **1**.

According to eqn (2) and (3),

$$d_{33} = 2\varepsilon_{33}Q_{33}P_s \quad (2)$$

$$g_{33} = d_{33}/\varepsilon_{33} = 2Q_{33}P_s \quad (3)$$

(where ε_{33}, Q_{33} and P_s are the dielectric permittivity, electrostrictive coefficient, and spontaneous polarization, respectively), it is clear that the large d_{33} and g_{33} are closely related to P_s and the electrostrictive coefficient (Q_{33}). Compared to multiaxial ferroelectrics with similar configurations, such as $[N(CH_3)_4]FeCl_4$,[23] $[N(CH_3)_4]GaCl_4$,[24] and $[N(CH_3)_3CH_2Cl]GaCl_4$,[16] the P_s of compound **1** surpasses those of the aforementioned compounds (Table S5†). According to Table S6,† it is clear that organic cations with larger dipole moments contribute to the enhancement of P_s. However, in contrast to P_s, d_{33} and g_{33}, eqn (2) and (3) indicate that the increase in $d_{33} \times g_{33}$ values cannot be solely attributed to the improvement in P_s, and Q_{33} also plays a crucial role. Distinctly, the flexible organic cation and multiaxial

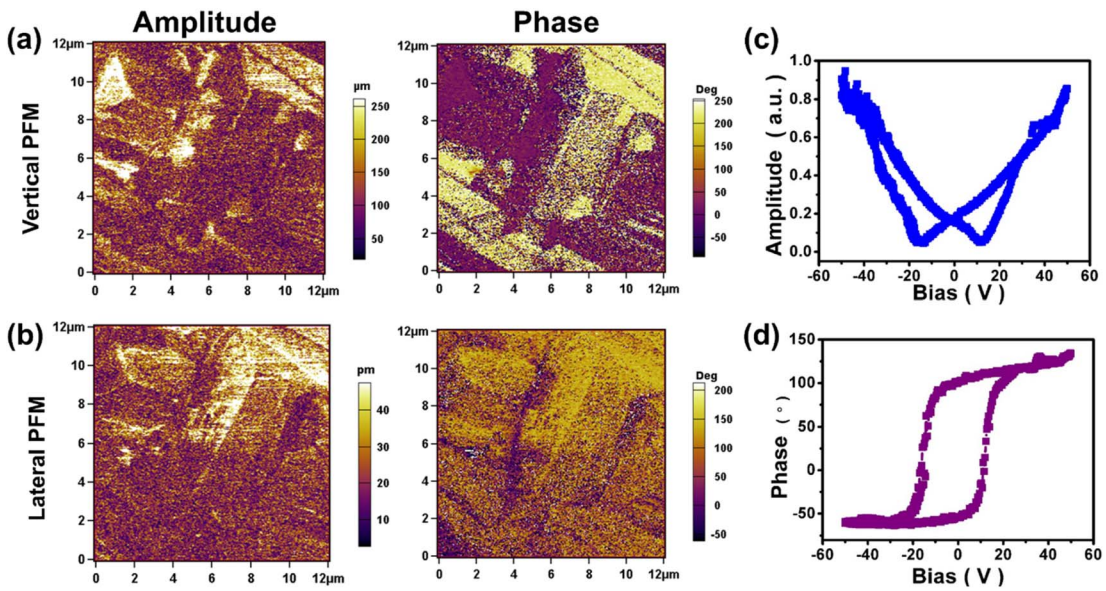

Fig. 3 Domain structure of **1**. Vertical (a) and lateral (b) PFM amplitude and phase images for a polycrystalline film of **1**; vertical PFM amplitude (c) and phase (d) signals as functions of the tip voltage for a selected point.

© 2024 The Author(s). Published by the Royal Society of Chemistry

Open Access Article. Published on 28 August 2024. Downloaded on 6/21/2025 3:22:39 AM. This article is licensed under a Creative Commons Attribution-NonCommercial 3.0 Unported Licence.

characteristics in **1** play an important role in the enhancement of its Q_{33}.[16,23,25–27] Therefore, the large $d_{33} \times g_{33}$ value observed in **1** indicates that using more flexible organic cations with larger dipole moments to construct molecule-based ferroelectrics with multiaxial characteristics is an effective way to obtain molecule-based ferroelectrics with large values.

Performance of the 1@PDMS PEG

Because **1** exhibited very large $d_{33} \times g_{33}$, the PEG was fabricated with a polymer composite film comprising particles of **1** and polydimethylsiloxane (PDMS) (**1**@PDMS) as the piezoelectric layer and conductive tape as the electrode (Fig. 5a). The particles of **1** were synthesized using the reversed-phase microemulsion method. The lengths and widths of the rods in **1** were in the ranges 7000–9000 nm and 1000–2000 nm, respectively (Fig. S12†). Polymer composite films (**1**@PDMS) with 5, 10, 15, 20, and 25 wt% contents for the particles of **1** were prepared by dispersing the corresponding quantities into PDMS with mechanical stirring. The morphology and cross-sectional scanning electron microscopy (SEM) and mapping images of chlorine (Cl), bromine (Br), and gallium (Ga) of compound **1** and silicon (Si) of PDMS revealed that the thickness of 15 wt% **1**@PDMS is ~300 μm and that the particles of **1** are uniformly dispersed within the PDMS matrix (Fig. 5b and S13†).

The PEG consisting of 3 cm × 3 cm **1**@PDMS composite films with an effective working surface area of 2 × 2 cm^2 is fabricated to measure the open circuit voltage (V_{oc}), the short-circuit current (I_{sc}) and the power density by applying a constant force of less than 20 N to the surfaces of the PEGs (Fig. S14†) with thumb pressure. As shown in Fig. 5c, the open circuit voltage (V_{oc}) increased with increasing concentration of **1** and reached saturation when the concentration of **1** was 15 wt%. Then, it decreased with increasing concentration of **1** owing to the presence of Maxwell–Wagner–Sillars polarization in the heterogeneous materials.[28–30] The short-circuit current (I_{sc}) showed the same trend as the open circuit voltage with an increase in the concentration of **1** (Fig. S15†). The maximum values for V_{oc} and I_{sc} were 179 V and 6.4 μA, respectively. These values are significantly larger than 42 V and 1.2 μA observed in the ground sample **1**@PDMS (Fig. S16†). Considering the morphological differences between particles **1** synthesized by the reversed-phase microemulsion method and the ground sample (Fig. S17†), the enhancement in outputs is mainly due to the morphological changes of the sample caused by high surface stress.[31] The peak values of V_{oc} for the forward and backward connections were completely reversed, confirming that the signal was generated by the piezoelectric effect (Fig. S18†). To further exclude the effect of PDMS, pure PDMS film samples were prepared and tested for V_{oc} and I_{sc}. Under identical conditions, the V_{oc} and I_{sc} values for these pure PDMS samples, matched in size, were 3.7 V and 25 nA, respectively (Fig. S19†). These results clearly indicate that the primary contribution to the output performance of the **1**@PDMS composite arises from the piezoelectric effect of **1**.

To evaluate the maximum power density of the 15 wt% **1**@PDMS composite, the PEG power density was measured across load resistances ranging from 1 to 10 MΩ. As illustrated in Fig. 5d, the maximum instantaneous power density reached 120 μW cm^{-2} at a load resistance of 3 MΩ. This represents the highest output power density among all known PEGs utilizing the same PDMS matrix (Table S7†). Significantly, the PEG consisting of 10 cm × 10 cm **1**@PDMS composite films with an effective working surface area of 8 × 8 cm^2 was connected with a full-wave rectifying bridge and light-emitting diodes (LEDs) in the circuit (Fig. S20a†) and successfully powered 100 LEDs connected in series, as shown in Fig. 6a. Additionally, a charge transfer circuit equipped with a full-wave rectifying bridge and a 3.3 μF parallel capacitor was utilized to operate a calculator and an electronic watch (Fig. S20b and c†). Notably, the 15 wt% **1**@PDMS PEG substitutes for the solar system to power the calculator, enabling it to perform various calculation tasks (Fig. 6b and Movie S1†). Similarly, it also drove an electronic watch to work continuously (Fig. 6c and Movie S2†). It is worth mentioning that the operating powers for commonly used portable electronic devices, such as watches, RFID tags, pacemakers and hearing aids, range from 3 to 100 μW.[32] Therefore, the **1**@PDMS PEG could be integrated into self-powered devices or battery chargers.

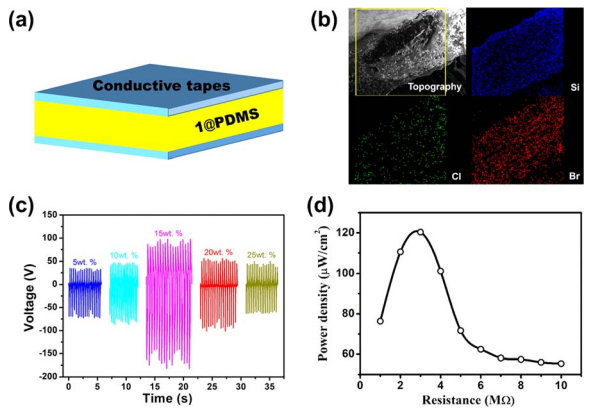

Fig. 5 Construction and performance of the PEG. (a) Schematic diagram of the PEG. (b) Cross-sectional scanning electron microscopy (SEM) and mapping images of 15 wt% **1**@PDMS. (c) V_{oc} for **1**@PDMS with different mass fractions with thumb pressure. (d) Power density as a function of load resistance for 15 wt% **1**@PDMS.

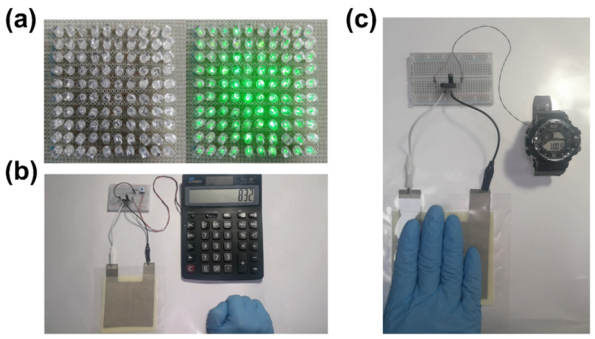

Fig. 6 PEG device application demonstration. Lighting LEDs (a), powering a commercial calculator (b) and a wearable electronic watch (c) by pressing 15 wt% **1**@PDMS PEGs.

Open Access Article. Published on 28 August 2024. Downloaded on 6/21/2025 3:22:39 AM. This article is licensed under a Creative Commons Attribution-NonCommercial 3.0 Unported Licence.

Conclusions

In summary, we have reported a molecule-based ferroelectric **1**, characterized by exceptionally high values of d_{33} (454 pC N^{-1}) and g_{33} (10 910 × 10^{-3} V m N^{-1}) simultaneously and the largest $d_{33} \times g_{33}$ (4953.1 × 10^{-12} m^2 N^{-1}) among all known free-standing polycrystalline pellets. Investigation on the piezoelectric properties of **1** revealed that employing more flexible organic cations with larger dipole moments to construct multiaxial molecule-based ferroelectrics is an effective way to obtain molecule-based ferroelectrics with large $d_{33} \times g_{33}$ values. Significantly, the **1**@PDMS PEG, composed of 15 wt% compound **1** and PDMS, achieved a power density of up to 120 μW cm^{-2} under a 20 N pressure applied with thumb pressure, marking the highest power density reported to date for any ferroelectric@PDMS PEG. This work therefore establishes a robust foundation for the practical application of molecule-based materials in flexible, self-powered power supplies.

Experimental

Synthesis of compound 1

All reagents and solvents are commercially available and of reagent grade purity for direct synthesis. Gallium(III) oxide (2 mmol) was first dissolved into HBr (40%) at 100 °C, and then (2-chloroethyl)trimethylammonium chloride (2 mmol) was dissolved in the above solution. The two solutions were mixed to obtain a clear, faint yellow solution. After the solution evaporated for weeks, faint yellow crystals of **1** were obtained (total yield: 85%, based on (2-chloroethyl)trimethylammonium chloride).

Preparation of particles of 1

A 330 mg mL^{-1} aqueous solution of **1** was slowly dripped into 30 mL of isopropyl alcohol with ultrasonic stirring at room temperature. During mixing, the colorless solution turned into an emulsion, indicating particle formation. The particles were purified by centrifugation at 8500 rpm for 2–3 min and then redissolved in 1 mL of toluene to prepare the composite film.

Preparation of 1@PDMS composite films

A PDMS solution was composed of primary and secondary liquids with toluene stirred in a ratio of 10 : 1 : 11 in a 50 mL beaker. Then, **1** was dispersed in toluene in various proportions (5, 10, 15, 20 and 25 wt%) and mixed with PDMS solutions. The prepared solution was evenly spread in a Teflon evaporator with a diameter of 60 mm and then cured at 373 K for 2 h in an ambient atmosphere.

Fabrication of PEGs

First, 6 cm diameter **1**@PDMS composite films were sliced into 3 cm × 3 cm squares. Subsequently, the sheared **1**@PDMS composite films were inserted between two conductive cloth tape electrodes, each sized 2 cm × 6 cm and coated with a conductive tape electrode (a polyester, metallized with Cu and Ni), to fabricate a sandwich structure device. The effective working area of the PEG device is 2 × 2 cm^2. Second, the sandwich structure of the conductive tape electrode–**1**@PDMS composite films–conductive tape electrode was clamped using laminating pouches. Then, to improve contact between the conductive tape electrode and the films, the laminating pouches were pressed tightly with a commercial thermal laminator to eliminate air gaps. Using the above method, the PEG consisting of 10 cm × 10 cm **1**@PDMS composite films with an effective working surface area of 8 × 8 cm^2 is fabricated. Finally, the devices of **1**@PDMS were poled with 50 kV cm^{-1} for 30 min at room temperature.

PFM measurement

A commercial piezoresponse force microscope (Cypher, Asylum Research) was utilized to perform piezoresponse force microscopy (PFM) measurements with an AC driving voltage applied to the conductive tip. The domain imaging studies were conducted using conductive Pt/Ir-coated silicon probes (EFM-20, Nanoworld) with a nominal spring constant of ~2.8 N m^{-1} and a free-air resonance frequency of ~75 kHz. And a 20 μL aqueous solution of **1** with 20 mg mL^{-1} was gently evaporated onto freshly cleaned ITO-coated glass to prepare thin films. Then, the prepared sample was loaded and the head was positioned above the sample. The sum and deflection engaging the surface were set. After that, the driving voltage was configured (1.5 V) and the drive frequency was tuned (320 kHz, 670 kHz), as well as scanning parameters were set (2.44 Hz, 12 μm, 5 μm). At last, imaging parameters were set and imaging was started.

PEG performance measurement

The V_{oc}, I_{sc} and power density of PEGs of **1**@PDMS were measured using a Keithley electrometer (6517B). The outputs of the PEGs were measured by applying a constant force of less than 20 N and approximately 2 Hz to the surfaces of the PEGs with thumb pressure. The PEG power density was obtained through measuring the output current of various load resistances ranging from 1 to 10 MΩ under the same applied force conditions.

Details of the XRD, TG, SHG, d_{33}, *S*–*E* curve, dielectric constant, and *P*–*E* curve measurements are provided in the ESI.†

Data availability

The data supporting this article have been included as part of the ESI.†

Author contributions

H. X. Z., L. S. L. and L. S. Z. conceived the idea and designed the project. B. W. and Z. R. L. grew the single crystals and prepared the devices, carried out the PFM, ferroelectric, piezoelectric, dielectric, and TG measurements, and analyzed the results with H. X. Z. and L. S. L. Z. R. L performed the powder XRD measurements and conducted the powder XRD analysis. Z. X. T.

© 2024 The Author(s). Published by the Royal Society of Chemistry

Open Access Article. Published on 28 August 2024. Downloaded on 6/21/2025 3:22:39 AM. This article is licensed under a Creative Commons Attribution-NonCommercial 3.0 Unported Licence.

contributed to sample preparation. B. W., Z. R. L., H. X. Z. and L. S. L. wrote the manuscript with input from all the authors. All authors discussed the results and commented on the manuscript.

Conflicts of interest

There are no conflicts to declare.

Acknowledgements

The authors thank Prof. Ren-Gen Xiong, Wei-Qiang Liao and Xian-jiang Song (Nanchang University) for their assistance and suggestions. This work was supported by the National Natural Science Foundation of China (grant no. 22371235, 92161203, and 92361301).

Notes and references

1 W. Q. Liao, D. Zhao, Y. Y. Tang, Y. Zhang, P. F. Li, P. P. Shi, X. G. Chen, Y. M. You and R. G. Xiong, *Science*, 2019, **363**, 1206–1210.
2 G. G. Huang, A. A. Khan, M. M. Rana, C. Xu, S. Xu, R. Saritas, S. Zhang, E. Abdel-Rahmand, P. Turban, S. Ababou-Girard, C. Wang and D. Y. Ban, *ACS Energy Lett.*, 2020, **6**, 16–23.
3 K. Dong, X. Peng and Z. L. Wang, *Adv. Mater.*, 2020, **32**, 1902549.
4 Y. Jiang, K. Dong, J. An, F. Liang, J. Yi, X. Peng, C. Ning, C. Ye and Z. L. Wang, *ACS Appl. Mater. Interfaces*, 2021, **13**, 11205–11214.
5 Z. Lou, L. Li, L. Wang and G. Shen, *Small*, 2017, **13**, 1701791.
6 Z. Li, H. C. Thong, Y. F. Zhang, Z. Xu, Z. Zhou, Y. X. Liu, Y. Y. S. Cheng, S. H. Wang, C. Zhao, F. Chen, K. Bi, B. Han and K. Wang, *Adv. Funct. Mater.*, 2020, **31**, 2005012.
7 Y. Saito, H. Takao, T. Tani, T. Nonoyama, K. Taktori, T. Homma, T. Nagaya and M. Nakamura, *Nature*, 2004, **432**, 81–84.
8 K. Uchino, *Piezoelectric Actuators and Ultrasonic Motors*, Springer, New York, 1996.
9 Z. Z. Liu, S. S. Li, J. Z. Zhu, L. W. Mi and G. Q. Zheng, *ACS Appl. Mater. Interfaces*, 2022, **14**, 11854–11863.
10 M. P. Zheng, Y. D. Hou, M. K. Zhu and H. Yan, *J. Chin. Ceram. Soc.*, 2016, **44**, 359–366.
11 V. Bijalwan, J. Erhart, Z. Spotz, D. Sobola, V. Prajzler, P. Tofel and K. Maca, *J. Am. Ceram. Soc.*, 2020, **104**, 1088–1101.
12 I. T. Seo, C. H. Choi, D. Song, M. S. Jang, B. Y. Kim, S. Nahm, Y. S. Kim, T. H. Sung, H. C. Song and S. Zhang, *J. Am. Ceram. Soc.*, 2013, **96**, 1024–1028.
13 Y. X. Gao, C. R. Qiu, G. Li, M. Ma, S. Yang, Z. Xu and F. Li, *Appl. Energy*, 2020, **271**, 115193.
14 T. Vijayakanth, D. J. Liptrot, E. Gazit, R. Boomishankar and C. R. Bowen, *Adv. Funct. Mater.*, 2022, **32**, 2109492.
15 X. G. Chen, X. J. Song, Z. X. Zhang, P. F. Li, J. Z. Ge, Y. Y. Tang, J. X. Gao, W. Y. Zhang, D. W. Fu, Y. M. You and R. G. Xiong, *J. Am. Chem. Soc.*, 2020, **142**, 1077–1082.
16 B. Wang, J. F. Hong, Y. T. Yang, H. X. Zhao, L. S. Long and L. S. Zheng, *Matter*, 2022, **5**, 1296–1304.
17 Y. Liu, B. Zhang, W. Xu, A. Haibibu, Z. Han, W. Lu, J. Bernholc and Q. Wang, *Nat. Mater.*, 2020, **19**, 1169–1174.
18 Q. M. Zhang, V. Bharti and X. Zhao, *Science*, 1998, **280**, 2101–2104.
19 L. Jin, J. Pang, Y. Pu, N. Xu, Y. Tian, R. Jing, H. Du, X. Wei, Z. Xu, D. Guo, J. Xu and F. Gao, *Ceram. Int.*, 2019, **45**, 22854–22861.
20 C. W. Ahn, G. Choi, I. W. Kim, J. S. Lee, K. Wang, Y. Hwang and W. Jo, *NPG Asia Mater.*, 2017, **9**, e346.
21 Z. Hu, K. Parida, H. Zhang, X. Wang, Y. Li, X. Zhou, S. A. Morris, W. H. Liew, H. Wang, T. Li, F. Jiang, M. Yang, M. Alexe, Z. Du, C. L. Gan, K. Yao, B. Xu, P. S. Lee and H. J. Fan, *Nat. Commun.*, 2022, **13**, 5607.
22 M. Y. Li, H. J. Wondergem, M. J. Spijkman, K. Asadi, I. Katsouras, P. W. Blom and D. M. de Leeuw, *Nat. Mater.*, 2013, **12**, 433–438.
23 J. Harada, N. Yoneyama, S. Yokokura, Y. Takahashi, A. Miura, N. Kitamura and T. Inabe, *J. Am. Chem. Soc.*, 2018, **140**, 346–354.
24 D. Li, X. M. Zhao, H. X. Zhao, X. W. Dong, L. S. Long and L. S. Zheng, *Adv. Mater.*, 2018, **30**, 1803716.
25 Y. Z. Hu, L. You, B. Xu, T. Li, S. A. Morris, Y. X. Li, Y. H. Zhang, X. Wang, P. S. Lee, H. J. Fan and J. L. Wang, *Nat. Mater.*, 2021, **20**, 612–617.
26 J. Harada, Y. Kawamura, Y. Takahashi, Y. Uemura, T. Hasegawa, H. Taniguchi and K. Maruyama, *J. Am. Chem. Soc.*, 2019, **141**, 9349–9357.
27 Y. X. Gao, M. H. Wu and P. Jena, *Nat. Commun.*, 2021, **12**, 1331.
28 R. Ding, H. Liu, X. L. Zhang, J. X. Xiao, R. Kishor, H. X. Sun, B. W. Zhu, G. Chen, F. Gao, X. H. Feng, J. S. Chen, X. D. Chen, X. W. Sun and Y. J. Zheng, *Adv. Funct. Mater.*, 2016, **26**, 7708–7716.
29 M. Arous, H. Hammami, M. Lagache and A. Kallel, *J. Non-Cryst. Solids*, 2007, **353**, 4428–4431.
30 S. Ippili, V. Jella, J. Kim, S. Hong and S. G. Yoon, *ACS Appl. Mater. Interfaces*, 2020, **12**, 16469–16480.
31 A. A. Khan, G. Huang, M. M. Rana, N. Q. Mei, M. Biondi, S. Rassel, N. Tanguy, B. Sun, Z. Leonenko, N. Yan, C. L. Wang, S. H. Xu and D. Y. Ban, *Nano Energy*, 2021, **86**, 106039.
32 E. L. Pradeesh, S. Udhayakumar, M. G. Vasundhara and G. K. Kalavathi, *Microsyst. Technol.*, 2022, **28**, 1797–1830.

© 2024 The Author(s). Published by the Royal Society of Chemistry